# Toward Sensorless Interaction Force Estimation for Industrial Robots Using High-Order Finite-Time Observers

Linyan Han, Jianliang Mao, *Member, IEEE*, Pengfei Cao, Yahui Gan, and Shihua Li, *Fellow, IEEE*

***Abstract*—This article proposes a novel interaction force estimation scheme capable of estimating the interaction forces for industrial robots with high precision in the absence of force sensors. Specifically, we first establish the dynamic model of a class of industrial robots via model identification methods. Furthermore, a high-order finite-time observer (HOFTO) is established to estimate the interaction forces, where HOFTO serves as an interaction force observer and is designed to accurately estimate external time-varying interaction forces. In addition, we strictly analyze the stability of our approach in two different cases, endowing HOFTO with reliable estimation abilities in broader applications. Subsequently, we integrate the estimated force information into the applications of force control frameworks (e.g., collision detection and impedance control). Several evaluations on a real 6-axes robot demonstrate the effectiveness of the proposed approach.**

***Index Terms*—Force control, high-order finite-time observer, interaction force estimation, parameter identification.**

## I. Introduction

In A myriad of applications, such as deburring [1] and guiding tasks [2] as well as collision detection [3], robot manipulators need to contact with external environments properly and thus careful treatment of interaction forces is vital. In force-sensitive scenarios, traditional approaches on position control are prone to impose strong stiffness using large control gains and consequently the risk of breaking robots and harming environments becomes high. In order to overcome this issue of position-control methods, force control has been studied toward obtaining an environment or user-friendly controller, where interaction forces between robots and the environment are taken into account. Usually, interaction forces are measured by a force/torque sensor. However, the high price of force sensors restricts their applicability in various settings. Moreover, the deployment of force sensors per se also increases the difficulty of structural design. Therefore, an efficient and easily implemented interaction force observer has great potentials, which indeed has been showcased in many previous works [4]–[6].

A straightforward way of estimating interaction forces is to utilize the motor torque, position, velocity, and acceleration information [7]. However, this kind of approaches will become problematic since double differentiation of position signals amplifies measurement noise in practice. Therefore, various filters [8] were employed to improve the estimation accuracy of interaction forces, which, however, brings another issue, i.e., the small time delay caused by the filter will prolong the system's response time.

In order to address the aforementioned issues, many alternative solutions have been investigated [9]–[12]. In [9], a nonlinear disturbance observer was proposed to estimate the interaction forces. The stability and performance of the reaction torque observer in a robust force control system were analyzed, where the estimation of environmental impedance control through the reaction torque observer can be viewed as an application of disturbance observers [10], [11]. In [12], an extended state observer (ESO) was applied to estimate the interaction forces with a theoretical analysis. However, these works only focus on estimating constant or slow time-varying interaction forces while the case of fast time-varying interaction forces (e.g., in highly dynamical environments) has not been explored sufficiently.

Based on the design idea of finite time convergence, the super-twisting algorithm (STA) observer [13] is designed to estimate the interaction forces and has achieved great success. However, the STA observer is first order and can only accurately estimate the interaction forces with the first-order derivative bounded. However, the interaction forces in practice are complex and changeable, so it is desired to design an interaction force observer with the ability of generalization.

Manuscript received December 31, 2020; revised April 23, 2021 and June 8, 2021; accepted June 22, 2021. Date of publication July 14, 2021; date of current version February 9, 2022. This work was supported in part by the National Natural Science Foundation (NNSF) of China under Grant 61973081, Grant 62025302, and Grant 61873308, in part by the Fundamental Research Funds for the Central Universities under Grant 202008003, and in part by the Key R & D plan of Jiangsu Province under Grant BE2020082-4. *(Corresponding author: Shihua Li.)*

Linyan Han, Pengfei Cao, Yahui Gan, and Shihua Li are with the School of Automation, Key Laboratory of Measurement and Control of Complex Systems of Engineering, Ministry of Education, Southeast University, Nanjing 210096, China (e-mail: ly.han@seu.edu.cn; pengfei_cao@seu.edu.cn; y.h.gan@seu.edu.cn; lsh@seu.edu.cn).

Jianliang Mao is with the College of Automation Engineering, Shanghai University of Electric Power, Shanghai 200090, China and also with the R & D Institute of Estun Automation Company, Ltd., Nanjing 211106, China (e-mail: jl_mao@shiep.edu.cn).

Color versions of one or more figures in this article are available at https://doi.org/10.1109/TIE.2021.3095820.

Digital Object Identifier 10.1109/TIE.2021.3095820

In this article, we are dedicated to design a force observer so as to estimate time-varying (particularly fast time-varying) interaction forces, with the aim of addressing the limitations of the aforementioned approaches. Specifically, using an identified dynamics model of robot manipulators, we design a HOFTO to estimate the interaction forces in a finite time horizon. The proposed interaction force observer not only guarantees the global stability, but also provides a more accurate estimation in comparison with the traditional ESO-based methods. The main contributions of this article include the following.

1) *An observer design method is utilized to achieve the sensorless interaction force estimation, which is better than traditional direct estimation methods and ESO-based methods in terms of estimation accuracy [12].*
2) *A finite-time observer is designed to estimate the interaction forces with rigorous stability analysis.*

This article is arranged as follows. The motivation of our work is first explained in Section II. Then, we illustrate the design procedure of the interaction force observer in detail in Section III. Several experiments on a real robot are reported in Section IV. Finally, we conclude this article in Section V.

## II. Motivation

In this section, we discuss the existing interaction force estimation methods and their shortcomings, which motivate our work to cope with these issues.

### A. Direct Estimation of $\boldsymbol{\tau}_e$

As a well-established model, the Euler–Lagrange equation [14] has been widely employed to represent the dynamics of robots. Specifically, for a robot manipulator with $r$-$link$, its dynamic model can be described as

$$\mathbf{M}(\mathbf{q})\ddot{\mathbf{q}} + \mathbf{C}(\mathbf{q},\dot{\mathbf{q}}) + \mathbf{g}(\mathbf{q}) + \mathbf{f} = \boldsymbol{\tau} + \boldsymbol{\tau}_e \tag{1}$$

where $\mathbf{q} \in \mathbb{R}^{r\times 1}$, $\dot{\mathbf{q}}$ and $\ddot{\mathbf{q}}$ denote joint position, velocity, and acceleration, respectively. $\mathbf{M}(\mathbf{q}) \in \mathbb{R}^{r\times r}$ is a symmetric, positive-definite matrix, $\mathbf{C}(\mathbf{q},\dot{\mathbf{q}}) \in \mathbb{R}^{r\times 1}$ represents Coriolis and centrifugal terms, $\mathbf{g}(\mathbf{q}) \in \mathbb{R}^{r\times 1}$ denotes gravity, $\mathbf{f} \in \mathbb{R}^{r\times 1}$ represents friction force, $\boldsymbol{\tau}_e \in \mathbb{R}^{r\times 1}$ denotes the interaction force (which will be estimated in this article without using a torque/force sensor) and $\boldsymbol{\tau} \in \mathbb{R}^{r\times 1}$ denotes joint torque (which is also referred to as control input).

According to (1), the direct estimation can be calculated as

$$\hat{\boldsymbol{\tau}}_e = \mathbf{M}(\mathbf{q})\ddot{\mathbf{q}} + \mathbf{C}(\mathbf{q},\dot{\mathbf{q}}) + \mathbf{g}(\mathbf{q}) + \mathbf{f} - \boldsymbol{\tau} \tag{2}$$

with $\hat{\boldsymbol{\tau}}_e$ being the estimation of $\boldsymbol{\tau}_e$.

Note that in (2), $\mathbf{q}$, $\dot{\mathbf{q}}$, $\ddot{\mathbf{q}}$, and $\boldsymbol{\tau}$ are needed to calculate the interaction force. However, in practice, only the joint positions $\mathbf{q}$, joint velocity $\dot{\mathbf{q}}$ and $\boldsymbol{\tau}$ can be obtained from the servo drive. A simple solution to estimate $\ddot{\mathbf{q}}$ is to resort to the second-order differentiators, which, however, will amplify the noise introduced during the measurement signals.

### B. Indirect Estimation of $\boldsymbol{\tau}_e$ Though Traditional Extended State Observer

In this subsection, we will show the ESO-based interaction force estimation approach and its shortcomings.

Define $\mathbf{x}_1 = \mathbf{q}$, $\mathbf{x}_2 = \dot{\mathbf{q}}$ and $\mathbf{x}_3 = \mathbf{M}(\mathbf{x}_1)^{-1}\boldsymbol{\tau}_e$. The dynamic model in (1) becomes

$$\begin{cases} \dot{\mathbf{x}}_1 = \mathbf{x}_2, \\ \dot{\mathbf{x}}_2 = \mathbf{M}(\mathbf{x}_1)^{-1}\boldsymbol{\tau} + \mathbf{F}(\mathbf{x}_1,\mathbf{x}_2) + \mathbf{x}_3 \end{cases} \tag{3}$$

where the nonlinear function $\mathbf{F}(\mathbf{x}_1,\mathbf{x}_2) \in \mathbb{R}^{r\times 1}$ is defined as

$$\mathbf{F}(\mathbf{x}_1,\mathbf{x}_2) = -\mathbf{M}(\mathbf{x}_1)^{-1}\left(\mathbf{C}(\mathbf{x}_1,\mathbf{x}_2) + \mathbf{g}(\mathbf{x}_1) + \mathbf{f}\right). \tag{4}$$

The standard ESO can be designed to estimate the interaction force, i.e.,

$$\begin{cases} \dot{\mathbf{z}}_1 = \mathbf{z}_2 + \mathbf{k}_1(\mathbf{x}_1 - \mathbf{z}_1) \\ \dot{\mathbf{z}}_2 = \mathbf{M}(\mathbf{x}_1)^{-1}\boldsymbol{\tau} + \mathbf{F}(\mathbf{x}_1,\mathbf{x}_2) + \mathbf{z}_3 + \mathbf{k}_2(\mathbf{x}_1 - \mathbf{z}_1) \\ \dot{\mathbf{z}}_3 = \mathbf{k}_3(\mathbf{x}_1 - \mathbf{z}_1) \\ \hat{\boldsymbol{\tau}}_e = \mathbf{M}(\mathbf{x}_1)\mathbf{z}_3 \end{cases} \tag{5}$$

where $\mathbf{k}_i \in \mathbb{R}^{r\times r}$, $\mathbf{z}_i$, $i = \{1,2,3\}$, and $\hat{\boldsymbol{\tau}}_e$ represent design parameters, the estimation of system states $\mathbf{x}_i$, and the estimation of $\boldsymbol{\tau}_e$, respectively.

Denote $\mathbf{e}_1 = \mathbf{x}_1 - \mathbf{z}_1$, $\mathbf{e}_2 = \mathbf{x}_2 - \mathbf{z}_2$, $\mathbf{e}_3 = \mathbf{x}_3 - \mathbf{z}_3$ and $\mathbf{e} = \begin{bmatrix}\mathbf{e}_1^{\mathrm{T}} & \mathbf{e}_2^{\mathrm{T}} & \mathbf{e}_3^{\mathrm{T}}\end{bmatrix}^{\mathrm{T}}$. Combining (3) with (5) yields the error dynamics as

$$\dot{\mathbf{e}} = \mathbf{A}\mathbf{e} + \mathbf{B}\dot{\mathbf{x}}_3 \tag{6}$$

with

$$\mathbf{A} = \begin{bmatrix} -\mathbf{k}_1 & \mathbf{I}_{r\times r} & \mathbf{0}_{r\times r} \\ -\mathbf{k}_2 & \mathbf{0}_{r\times r} & \mathbf{I}_{r\times r} \\ -\mathbf{k}_3 & \mathbf{0}_{r\times r} & \mathbf{0}_{r\times r} \end{bmatrix}, \mathbf{B} = \begin{bmatrix} \mathbf{0}_{r\times r} \\ \mathbf{0}_{r\times r} \\ \mathbf{I}_{r\times r} \end{bmatrix}. \tag{7}$$

Generally, it is trivial to select suitable parameters $\mathbf{k}_i, i = \{1,2,3\}$ to ensure that $\mathbf{A}$ is a Hurwitz matrix. Following (6), we have

$$\mathbf{e}(t) = \mathbf{e}^{\mathbf{A}t}\mathbf{e}(0) + \int_0^t \mathbf{e}^{\mathbf{A}(t-\iota)}\mathbf{B}\dot{\mathbf{x}}_3(\iota)d\iota. \tag{8}$$

Note that if $\dot{\mathbf{x}}_3 = \mathbf{0}$, we have $\mathbf{e}(\infty) = \dot{\mathbf{e}}(\infty) = \mathbf{0}$ since $\mathbf{A}$ is a Hurwitz matrix. This implies that ESO can accurately estimate constant or slowly time-varying lumped interaction forces; however, the estimation of nonconstant lumped interaction forces is not addressed therein. Suppose that the lumped interaction force $\mathbf{x}_3$ in (3) is nonconstant but bounded and with a bounded derivative, i.e., $\|\dot{\mathbf{x}}_3\| < \zeta, \zeta > 0$. Then, (8) can be transformed into

$$\|\mathbf{e}(t)\| \le \|\mathbf{e}^{\mathbf{A}t}\|\|\mathbf{e}(0)\| + \|\mathbf{A}^{-1}(\mathbf{I} - \mathbf{e}^{\mathbf{A}t})\mathbf{B}\|\zeta. \tag{9}$$

Taking the limit of (9) yields

$$\|\mathbf{e}(\infty)\| \le \|\mathbf{A}^{-1}\mathbf{B}\|\zeta. \tag{10}$$

Hence, the ESO introduces steady-state estimation errors in the presence of nonconstant lumped interaction forces. Refer to [15]

for a more detailed discussion on the ESO. This is also the motivation driving us to study a more efficient and accurate observer to estimate time-varying and nonconstant interaction forces.

## III. Main Results

Before proceeding to present our main results, some key notations and lemma are first introduced.

*Notations:* $\mathbf{x} = \left[x_1, x_2, \ldots, x_n\right]^{\mathrm{T}}$ denotes an $n$-dimensional vector with $x_i$ being the $i$th element of $\mathbf{x}$, where $i = 1, 2, \ldots, n$. $\mathrm{sig}^{\alpha}(\mathbf{x}) = \left[|x_1|^{\alpha}\mathrm{sign}(x_1), |x_2|^{\alpha}\mathrm{sign}(x_2), \ldots, |x_n|^{\alpha}\mathrm{sign}(x_n)\right]^{\mathrm{T}}$ with $\alpha > 0$. $\mathbf{x}^{\alpha} = \left[x_1^{\alpha}, x_2^{\alpha}, \ldots, x_n^{\alpha}\right]^{\mathrm{T}}$.

*Lemma 1 ([16]):* Let $c, d > 0$. For any $a > 0$, the following inequality holds for $\forall x, y \in \mathbb{R}$ : $|x|^c|y|^d \leq \frac{c}{c+d}a|x|^{c+d} + \frac{d}{c+d}a^{\frac{-c}{d}}|y|^{c+d}$.

### A. System Identification

In this subsection, we first build the dynamic model of industrial robots by the parameter identification method so as to facilitate the design of high-order finite-time observers in the next subsection.

During the process of identification, we assume that no external interaction forces are applied to the robot manipulator and therefore $\boldsymbol{\tau}_e$ is set as zero, i.e.,

$$\boldsymbol{\tau}_e = \mathbf{0}. \tag{11}$$

Usually, the friction model of the $i$th joint is described by [17]

$$f_i = Fc_i \cdot \mathrm{sign}(\dot{q}_i) + Fv_i\dot{q}_i + B_i \tag{12}$$

where $f_i$ is the $i$th element of $\mathbf{f}$, $Fc_i$ and $Fv_i$, respectively, denote the Coulomb and viscous friction coefficients, and $B_i$ is the bias term.

*Remark 1:* For the friction model, we only consider two conventional dynamics (e.g., Coulomb and viscous friction) since it is effective for our robot. In order to better characterize the friction, as future work, the improved friction models [18]–[20] can be used to generalize our results to other robots.

Due to the linearity in the parameters property [14], the inverse dynamic model in (1) can be written as

$$\boldsymbol{\tau} = \mathbf{H}_s(\mathbf{q}, \dot{\mathbf{q}}, \ddot{\mathbf{q}})\boldsymbol{\theta}_s \tag{13}$$

where $\mathbf{H}_s(\mathbf{q}, \dot{\mathbf{q}}, \ddot{\mathbf{q}}) \in \mathbb{R}^{r\times s}$ is called a regressor function and $\boldsymbol{\theta}_s \in \mathbb{R}^{s\times 1}$ represents the standard parameters. For rigid robot manipulators, there are 14 standard parameters for each joint and link, including six components ($I_{xxj}$ $I_{xyj}$ $I_{xzj}$ $I_{yyj}$ $I_{yzj}$ $I_{zzj}$) of inertia tensor for each link $j$, first moments ($mx_j$, $my_j$, $mz_j$) of link $j$, mass $m_j$, total inertia moment $Ia_j$, and friction parameters $Fv_j$ $Fc_j$ $B_j$.

In accordance with [21] and [22], we can utilize the column linear dependency of $\mathbf{H}_s$ to regroup the standard parameters and therefore (13) can be rewritten as

$$\boldsymbol{\tau} = \mathbf{H}(\mathbf{q}, \dot{\mathbf{q}}, \ddot{\mathbf{q}})\boldsymbol{\mu} \tag{14}$$

where $\mathbf{H}(\mathbf{q}, \dot{\mathbf{q}}, \ddot{\mathbf{q}}) \in \mathbb{R}^{r\times p}$ corresponds to a subset of the maximum linear independent columns of $\mathbf{H}_s$ and $\boldsymbol{\mu} \in \mathbb{R}^{p\times 1}$ represents the base parameters.

*Remark 2:* For rigid robot manipulators, there are 14 standard parameters for each joint and link. If a robot has $r$ joints, the number of standard parameters are $14r$. Hence, $s = 14r$ and $p < s$.

Assuming that we have access to $N$ groups of experimental data $\{\mathbf{H}(\mathbf{q}_t, \dot{\mathbf{q}}_t, \ddot{\mathbf{q}}_t), \boldsymbol{\tau}_t\}_{t=1}^{N}$ along an excitation trajectory, we have

$$\mathcal{T} = \mathcal{H}\boldsymbol{\mu} \tag{15}$$

where $\mathcal{H} = [\mathbf{H}_1{}^{\mathrm{T}}\mathbf{H}_2{}^{\mathrm{T}}\cdots\mathbf{H}_N{}^{\mathrm{T}}]^{\mathrm{T}}$, $\mathcal{T} = [\boldsymbol{\tau}_1{}^{\mathrm{T}}\boldsymbol{\tau}_2{}^{\mathrm{T}}\cdots\boldsymbol{\tau}_N{}^{\mathrm{T}}]^{\mathrm{T}}$. Hence, $\boldsymbol{\mu}$ can be obtained using the least squares estimation [23], [24].

### B. Improved Estimation of $\boldsymbol{\tau}_e$ Though High-Order Finite-Time Observer

We construct a high-order finite-time observer to estimate the interaction forces, since it provides us with crucial characteristics in interaction force estimation, including estimation accuracy and continuity. In order to design a high-order finite-time observer, the system parameters are required in advance. By importing the identification result, the friction model $\mathbf{f}$ can be extracted. Subsequently, the system parameter matrices $\mathbf{M}(\mathbf{q})$, $\mathbf{C}(\mathbf{q}, \dot{\mathbf{q}})$ and $\mathbf{g}(\mathbf{q})$ are obtained via algebraic sorting as

$$\begin{cases} \mathbf{g}(\mathbf{q}) = \mathbf{H}(\mathbf{q}, \mathbf{0}, \mathbf{0})\boldsymbol{\mu} - \mathbf{f} \\ \mathbf{C}(\mathbf{q}, \dot{\mathbf{q}}) = \mathbf{H}(\mathbf{q}, \dot{\mathbf{q}}, \mathbf{0})\boldsymbol{\mu} - \mathbf{f} - \mathbf{g}(\mathbf{q}) \\ \mathbf{M}_i(\mathbf{q}) = \mathbf{H}(\mathbf{q}, \mathbf{0}, \mathbf{E}_i)\boldsymbol{\mu} - \mathbf{f} - \mathbf{g}(\mathbf{q}) \end{cases} \tag{16}$$

where $\mathbf{E}_i = [\underbrace{0, \ldots, 0}_{i-1}, 1, \underbrace{0, \ldots, 0}_{r-i}]^{\mathrm{T}}$, $i = 1, \ldots, r$ and $\mathbf{M}_i(\mathbf{q})$ represents the $i$th column of $\mathbf{M}(\mathbf{q})$.

Now, the HOFTO can be constructed to estimate the interaction force, which is designed as

$$\begin{cases} \dot{\mathbf{z}}_1 = \mathbf{z}_2 + \mathbf{L}_1\mathrm{sig}^{m_2}(\mathbf{x}_1 - \mathbf{z}_1) \\ \dot{\mathbf{z}}_2 = \mathbf{M}(\mathbf{x}_1)^{-1}\boldsymbol{\tau} + \mathbf{F}(\mathbf{x}_1, \mathbf{x}_2) + \mathbf{z}_3 \\ \qquad\quad +\mathbf{L}_2\mathrm{sig}^{m_3}(\mathbf{x}_1 - \mathbf{z}_1) \\ \dot{\mathbf{z}}_3 = \mathbf{z}_4 + \mathbf{L}_3\mathrm{sig}^{m_4}(\mathbf{x}_1 - \mathbf{z}_1) \\ \ldots \\ \dot{\mathbf{z}}_{n+2} = \mathbf{L}_{n+2}\mathrm{sig}^{m_{n+3}}(\mathbf{x}_1 - \mathbf{z}_1) \\ \hat{\boldsymbol{\tau}}_e = \mathbf{M}(\mathbf{x}_1)\mathbf{z}_3 \end{cases} \tag{17}$$

where $\mathbf{z}_1, \mathbf{z}_2, \mathbf{z}_3, \ldots, \mathbf{z}_{n+2}, \hat{\boldsymbol{\tau}}_e$ are estimations corresponding to $\mathbf{x}_1, \mathbf{x}_2, \mathbf{x}_3, \ldots, \mathbf{x}_3^{(n-1)}, \boldsymbol{\tau}_e$. $\mathbf{L}_1, \mathbf{L}_2, \ldots, \mathbf{L}_{n+2} \in \mathbb{R}^{r\times r}$ denote the parameter matrices to be designed. Note that both the numerator and denominator of $m_i$ are odd such that the notation $\mathbf{x}^{m_i} = \mathrm{sig}^{m_i}(\mathbf{x})$ holds, where $m_i = 1 + (i-1)\sigma, \sigma \in (-1/(n+2), 0), i = 1, 2, \ldots, n+3$.

*Remark 3:* In general, the estimated order is selected according to the physical interaction force model. For instance, one can achieve finite-time stability for the observer by choosing $n = 1, 2$, and 3 for the constant, ramp, and parabolic interaction forces, respectively. Similarly, a higher order $n$ can be selected to ensure the estimation accuracy of the more general order interaction forces (e.g., forces with the polynomial types), which

however is attained at the cost of an increasing computational burden. In practice, we first consider low-order cases and later increase the order properly if the corresponding estimation is unsatisfactory.

Denote $\bar{\mathbf{e}}_1 = \mathbf{x}_1 - \mathbf{z}_1, \bar{\mathbf{e}}_2 = \mathbf{x}_2 - \mathbf{z}_2, \bar{\mathbf{e}}_3 = \mathbf{x}_3 - \mathbf{z}_3, \ldots, \bar{\mathbf{e}}_{n+2} = \mathbf{x}_3^{(n-1)} - \mathbf{z}_{n+2}$. Combining (3) and (17), we have

$$\begin{cases} \dot{\bar{\mathbf{e}}}_1 = \bar{\mathbf{e}}_2 - \mathbf{L}_1 \bar{\mathbf{e}}_1^{m_2} \\ \dot{\bar{\mathbf{e}}}_2 = \bar{\mathbf{e}}_3 - \mathbf{L}_2 \bar{\mathbf{e}}_1^{m_3} \\ \dot{\bar{\mathbf{e}}}_3 = \bar{\mathbf{e}}_4 - \mathbf{L}_3 \bar{\mathbf{e}}_1^{m_4} \\ \cdots \\ \dot{\bar{\mathbf{e}}}_{n+2} = \mathbf{x}_3^{(n)} - \mathbf{L}_{n+2} \bar{\mathbf{e}}_1^{m_{n+3}} \end{cases}. \tag{18}$$

Redefine $\mathbf{e}_1 = \bar{\mathbf{e}}_1$, $\mathbf{e}_2 = \mathbf{L}_1^{-1}\bar{\mathbf{e}}_2$, $\mathbf{e}_3 = \mathbf{L}_2^{-1}\bar{\mathbf{e}}_3$, $\cdots$, $\mathbf{e}_{n+2} = \mathbf{L}_{n+1}^{-1}\bar{\mathbf{e}}_{n+2}$. Equation (18) can be written as

$$\begin{cases} \dot{\mathbf{e}}_1 = \mathbf{L}_1(\mathbf{e}_2 - \mathbf{e}_1^{m_2}) \\ \dot{\mathbf{e}}_2 = \mathbf{L}_1^{-1}\mathbf{L}_2(\mathbf{e}_3 - \mathbf{e}_1^{m_3}) \\ \dot{\mathbf{e}}_3 = \mathbf{L}_2^{-1}\mathbf{L}_3(\mathbf{e}_4 - \mathbf{e}_1^{m_4}) \\ \cdots \\ \dot{\mathbf{e}}_{n+2} = \mathbf{L}_{n+1}^{-1}\mathbf{x}_3^{(n)} - \mathbf{L}_{n+1}^{-1}\mathbf{L}_{n+2}\mathbf{e}_1^{m_{n+3}} \end{cases}. \tag{19}$$

Denote $\mathbf{K}_1 = \mathbf{L}_1, \mathbf{K}_2 = \mathbf{L}_1^{-1}\mathbf{L}_2, \mathbf{K}_3 = \mathbf{L}_2^{-1}\mathbf{L}_3, \ldots, \mathbf{K}_{n+2} = \mathbf{L}_{n+1}^{-1}\mathbf{L}_{n+2}$. Then, we can rewrite (19) as

$$\begin{cases} \dot{\mathbf{e}}_1 = \mathbf{K}_1(\mathbf{e}_2 - \mathbf{e}_1^{m_2}) \\ \dot{\mathbf{e}}_2 = \mathbf{K}_2(\mathbf{e}_3 - \mathbf{e}_1^{m_3}) \\ \dot{\mathbf{e}}_3 = \mathbf{K}_3(\mathbf{e}_4 - \mathbf{e}_1^{m_4}) \\ \cdots \\ \dot{\mathbf{e}}_{n+2} = -\mathbf{K}_{n+2}\mathbf{e}_1^{m_{n+3}} + \mathbf{L}_{n+1}^{-1}\mathbf{x}_3^{(n)} \end{cases}. \tag{20}$$

***1) Case 1:*** Estimation of $\mathbf{x}_3$ with time series polynomial form

The following assumption plays a key role in introducing the main result.

*Assumption 1:* The $n$ time derivatives of $\mathbf{x}_{3i}$ exist and satisfy $\mathbf{x}_{3i}^{(n)}(t) = 0$.

*Theorem 1:* For the robot manipulator system (3) under Assumption 1, if the interaction force observer is designed as (17), then the estimation error will converge to zero in a finite time.

*Proof:* For the error system (20), if $\mathbf{x}_3^{(n)} = \mathbf{0}$, then we follow the spirit of [25] that there is a Lyapunov function $V(\mathbf{e})$ such that

$$\dot{V}(\mathbf{e}) \le -\gamma V^{\alpha}(\mathbf{e}) \tag{21}$$

where

$$\gamma > 0, 0 < \alpha < 1$$

and

$$V(\mathbf{e}) = \sum_{j=1}^{n+2}\sum_{i=1}^{r}\int_{\mathbf{e}_{(j+1)i}^{m_j/m_{j+1}}}^{\mathbf{e}_{(j)i}} \left(s^{\frac{2-m_j}{m_j}} - \mathbf{e}_{(j+1)i}^{\frac{2-m_j}{m_{j+1}}}\right) ds.$$

Hence, we can conclude from (21) that the estimation error will converge to zero in a finite time [25].

***2) Case 2:*** Estimation of time-varying interaction forces

The stability of the interaction force observer is introduced by Theorem 2 with satisfying Assumption 2.

*Assumption 2:* The $n$ time derivatives of external interaction forces $\boldsymbol{\tau}_e(t)$ exist. We can derive that $\mathbf{x}_3$ is continuously differentiable and its high-order derivatives are bounded, i.e., $|\mathbf{x}_{3i}^{(n)}| \le \kappa_i, i = 1, 2, \ldots, n$.

*Remark 4:* Assumption 2 needed here is essentially made to guarantee the finite-time convergence of the proposed observer with rigorous stability analysis. From a theoretical point of view, the proposed observer is finite-time convergent. As for the susceptibility of the closed-loop system to noise, we do not consider it in this article. To our knowledge, no results have been reported on this topic. However, this problem deserves to be studied in the future.

*Theorem 2:* For the robot manipulator system (3) under Assumption 2, if the interaction force observer is designed as (17), then the estimation value will converge to a bounded region in a finite time.

*Proof:* Define $\mathbf{H}_{i,j}(\mathbf{e}_{j+1}, \mathbf{e}_j) = [\mathbf{e}_{j+1}^{\frac{1}{j\sigma+1}}]^{i\sigma+1} - [\mathbf{e}_j^{\frac{1}{(j-1)\sigma+1}}]^{i\sigma+1}$. Then, we have $\sum_{j=1}^{i}\mathbf{H}_{i,j} = \mathbf{e}_{i+1} - \mathbf{e}_1^{m_{i+1}}, i = 1, \ldots, n+2$. Hence, (20) can be rewritten as

$$\begin{cases} \dot{\mathbf{e}}_1 = \mathbf{K}_1\mathbf{H}_{1,1} \\ \dot{\mathbf{e}}_2 = \mathbf{K}_2(\mathbf{H}_{2,2} + \mathbf{H}_{2,1}) \\ \dot{\mathbf{e}}_3 = \mathbf{K}_3(\mathbf{H}_{3,3} + \mathbf{H}_{3,2} + \mathbf{H}_{3,1}) \\ \cdots \\ \dot{\mathbf{e}}_{n+2} = -\mathbf{K}_{n+2}(\mathbf{H}_{n+2,n+2} + \cdots + \mathbf{H}_{n+2,1}) \\ \qquad +\mathbf{L}_{n+1}^{-1}\mathbf{x}_3^{(n)} \end{cases}. \tag{22}$$

Here, we can construct the same Lyapunov function shown in (21). Then, the derivative of $V(\mathbf{e})$ along system (22) can be written

$$\begin{aligned} \dot{V}|_{(22)} \le & -\sum_{j=1}^{n+2}\sum_{i=1}^{r}|\mathbf{e}_{(j+1)i} - \mathbf{e}_{(j)i}^{m_{j+1}/m_j}|^{\frac{2+\sigma}{m_{j+1}}} \\ & + \sum_{i=1}^{r}\frac{\partial V(\mathbf{e})}{\partial \mathbf{e}_{(n+2)i}}\mathbf{L}_{(n+1)i}^{-1}\mathbf{x}_{3i}^{(n)} \\ \le & -\gamma V^{\alpha}(\mathbf{e}) + \sum_{i=1}^{r}\frac{\partial V(\mathbf{e})}{\partial \mathbf{e}_{(n+2)i}}\mathbf{L}_{(n+1)i}^{-1}\kappa_i \end{aligned} \tag{23}$$

where

$$\begin{aligned} \sum_{i=1}^{r}\frac{\partial V(\mathbf{e})}{\partial \mathbf{e}_{(n+2)i}} = & \sum_{i=1}^{r}\mathbf{e}_{(n+2)i}^{(2-m_{n+2})/m_{n+2}} \\ & - \sum_{i=1}^{r}\frac{2-m_{n+1}}{m_{n+2}}\mathbf{e}_{(n+2)i}^{\frac{2-m_{n+1}}{m_{n+2}}-1}\mathbf{e}_{(n+1)i} \\ & + \sum_{i=1}^{r}\frac{2-m_{n+1}}{m_{n+2}}\mathbf{e}_{(n+2)i}^{\frac{2-m_{n+1}}{m_{n+2}}-1}\mathbf{e}_{(n+2)i}^{\frac{m_{n+1}}{m_{n+2}}}. \end{aligned} \tag{24}$$

Considering

$$\begin{aligned} |\mathbf{e}_{(n+1)i} - \mathbf{e}_{(n+2)i}^{\frac{m_{n+1}}{m_{n+2}}}| \le & \, b|\mathbf{e}_{(n+1)i}^{\frac{m_{n+2}}{m_{n+1}}} - \mathbf{e}_{(n+2)i}|^{\frac{m_{n+1}}{m_{n+2}}} \\ & + b|\mathbf{e}_{(n+1)i}^{\frac{m_{n+2}}{m_{n+1}}} - \mathbf{e}_{(n+2)i}||\mathbf{e}_{(n+2)i}|^{\frac{m_{n+1}}{m_{n+2}}-1}, \end{aligned} \tag{25}$$

with $b > 0$ being a constant, then we have

$$|\mathbf{e}_{(n+2)i}^{\frac{2-m_{n+1}}{m_{n+2}}-1}(\mathbf{e}_{(n+1)i}-\mathbf{e}_{(n+2)i}^{\frac{m_{n+1}}{m_{n+2}}})| \leq b|\mathbf{e}_{(n+2)i}|^{\frac{2-m_{n+1}}{m_{n+2}}-1}|\mathbf{e}_{(n+1)i}^{\frac{m_{n+2}}{m_{n+1}}}-\mathbf{e}_{(n+2)i}|^{\frac{m_{n+1}}{m_{n+2}}} + b|\mathbf{e}_{(n+2)i}|^{\frac{2-m_{n+2}+\sigma}{m_{n+2}}}|\mathbf{e}_{(n+1)i}^{\frac{m_{n+2}}{m_{n+1}}}-\mathbf{e}_{(n+2)i}|. \tag{26}$$

Following Lemma 1, we have

$$b|\mathbf{e}_{(n+2)i}|^{\frac{2-m_{n+1}}{m_{n+2}}-1}|\mathbf{e}_{(n+1)i}^{\frac{m_{n+2}}{m_{n+1}}}-\mathbf{e}_{(n+2)i}|^{\frac{m_{n+1}}{m_{n+2}}} \leq b_1|\mathbf{e}_{(n+2)i}|^{\frac{2-m_{n+2}}{m_{n+2}}}+b_2|\mathbf{e}_{(n+1)i}^{\frac{m_{n+2}}{m_{n+1}}}-\mathbf{e}_{(n+2)i}|^{\frac{2-m_{n+2}}{m_{n+2}}} \tag{27}$$

and

$$b|\mathbf{e}_{(n+2)i}|^{\frac{2-m_{n+2}+\sigma}{m_{n+2}}}|\mathbf{e}_{(n+1)i}^{\frac{m_{n+2}}{m_{n+1}}}-\mathbf{e}_{(n+2)i}| \leq b_3|\mathbf{e}_{(n+2)i}|^{\frac{2+\sigma}{m_{n+2}}}+b_4|\mathbf{e}_{(n+1)i}^{\frac{m_{n+2}}{m_{n+1}}}-\mathbf{e}_{(n+2)i}|^{\frac{2+\sigma}{m_{n+2}}} \tag{28}$$

with $b_1 = b^{\frac{2-m_{n+1}-m_{n+2}}{2-m_{n+2}}}$, $b_2 = b^{\frac{m_{n+1}}{2-m_{n+2}}}$, $b_3 = b^{\frac{2-m_{n+2}+\sigma}{2+\sigma}}$ and $b_4 = b^{\frac{m_{n+2}}{2+\sigma}}$.

Combining (27) and (28), (26) can be rewritten as

$$|\mathbf{e}_{(n+2)i}^{\frac{2-m_{n+1}}{m_{n+2}}-1}(\mathbf{e}_{(n+1)i}-\mathbf{e}_{(n+2)i}^{\frac{m_{n+1}}{m_{n+2}}})| \leq b_1|\mathbf{e}_{(n+2)i}|^{\frac{2-m_{n+2}}{m_{n+2}}} + b_3|\mathbf{e}_{(n+2)i}|^{\frac{2+\sigma}{m_{n+2}}}+b_2|\mathbf{e}_{(n+1)i}^{\frac{m_{n+2}}{m_{n+1}}}-\mathbf{e}_{(n+2)i}|^{\frac{2-m_{n+2}}{m_{n+2}}} + b_4|\mathbf{e}_{(n+1)i}^{\frac{m_{n+2}}{m_{n+1}}}-\mathbf{e}_{(n+2)i}|^{\frac{2+\sigma}{m_{n+2}}}. \tag{29}$$

Hence, (24) can be rewritten as

$$\begin{aligned}\sum_{i=1}^{r}\frac{\partial V(\mathbf{e})}{\partial \mathbf{e}_{(n+2)i}} &\leq \sum_{i=1}^{r} b_5|\mathbf{e}_{(n+2)i}|^{\frac{2-m_{n+2}}{m_{n+2}}} + \sum_{i=1}^{r} b_6|\mathbf{e}_{(n+2)i}|^{\frac{2+\sigma}{m_{n+2}}} + \sum_{i=1}^{r} b_7|\mathbf{e}_{(n+1)i}^{\frac{m_{n+2}}{m_{n+1}}}-\mathbf{e}_{(n+2)i}|^{\frac{2-m_{n+2}}{m_{n+2}}} \\ &+ \sum_{i=1}^{r} b_8|\mathbf{e}_{(n+1)i}^{\frac{m_{n+2}}{m_{n+1}}}-\mathbf{e}_{(n+2)i}|^{\frac{2+\sigma}{m_{n+2}}} \\ &\leq \sum_{i=1}^{r} b_9|\mathbf{e}_{(n+2)i}|^{\frac{2+\sigma}{m_{n+2}}} + rb_5\frac{m_{n+3}}{2+\sigma} \\ &+ \sum_{i=1}^{r} b_{10}|\mathbf{e}_{(n+1)i}^{\frac{m_{n+2}}{m_{n+1}}}-\mathbf{e}_{(n+2)i}|^{\frac{2+\sigma}{m_{n+2}}} + rb_7\frac{m_{n+3}}{2+\sigma}\end{aligned} \tag{30}$$

with $b_5 = \frac{2-m_{n+1}}{m_{n+2}}b_1 + 1$, $b_6 = \frac{2-m_{n+1}}{m_{n+2}}b_3$, $b_7 = \frac{2-m_{n+1}}{m_{n+2}}b_2$, $b_8 = \frac{2-m_{n+1}}{m_{n+2}}b_4$, $b_9 = b_5\frac{2-m_{n+2}}{2+\sigma} + b_6$, and $b_{10} = b_7\frac{2-m_{n+2}}{2+\sigma} + b_8$.

Then, according to the result in (30), (23) can be written as

$$\begin{aligned}\dot{V}|_{(22)} &\leq -\gamma V^{\alpha}(\mathbf{e}) + \sum_{i=1}^{r}\frac{\partial V(\mathbf{e})}{\partial \mathbf{e}_{(n+2)i}}\mathbf{L}_{(n+1)i}^{-1}\kappa_i \\ &\leq -\gamma V^{\alpha}(\mathbf{e}) + \sum_{i=1}^{r} b_9\mathbf{L}_{(n+1)i}^{-1}\kappa_i|\mathbf{e}_{(n+2)i}|^{\frac{2+\sigma}{m_{n+2}}} \\ &+ \sum_{i=1}^{r} b_{10}\mathbf{L}_{(n+1)i}^{-1}\kappa_i|\mathbf{e}_{(n+1)i}^{\frac{m_{n+2}}{m_{n+1}}}-\mathbf{e}_{(n+2)i}|^{\frac{2+\sigma}{m_{n+2}}} \\ &+ \sum_{i=1}^{r}\mathbf{L}_{(n+1)i}^{-1}\kappa_i b_5\frac{m_{n+3}}{2+\sigma} + \sum_{i=1}^{r}\mathbf{L}_{(n+1)i}^{-1}\kappa_i b_7\frac{m_{n+3}}{2+\sigma} \\ &\leq -\gamma V^{\alpha}(\mathbf{e}) + \gamma_1 V^{\alpha}(\mathbf{e}) + \Theta = -\rho V^{\alpha}(\mathbf{e}) + \Theta\end{aligned} \tag{31}$$

where $\rho = \gamma - \gamma_1 > 0, \gamma_1 = \max\{b_9\mathbf{L}_{(n+1)i}^{-1}\kappa_i, b_{10}\mathbf{L}_{(n+1)i}^{-1}\kappa_i\}$, $i = 1, 2, \ldots, r$ and $\Theta > 0$ are constant.

According to (31), we can conclude that the estimation value will converge to a bounded region $\Omega$ in a finite time, where

$$\Omega = \left\{\mathbf{e}_i \mid V(\mathbf{e}) \leq \left(\frac{\Theta}{\rho}\right)^{\frac{1}{\alpha}}, i = 1, 2, \ldots, n+2\right\}. \tag{32}$$

This completes the proof. ■

*Remark 5:* Generally, the estimation error of HOFTO can be reduced by increasing gain-related parameters $\mathbf{L}_i, i = 1, 2, \ldots, n+2$; however, it is noted that too large $\mathbf{L}_i$ will bring some other issues, such as noise amplification and overshoot. Therefore, in this case, we can also adjust the fractional power $\alpha$ to reduce the estimation error, which outperforms the ESO.

*Remark 6:* The HOFTO exhibits the advantage over the ESO [12] in terms of estimation accuracy. Unlike the ESO that can only accurately estimate constant or slowly time-varying interaction forces, the estimation accuracy for the fast time-varying interaction forces is not as high as the HOFTO.

*Remark 7:* In (17), if all of fractional power terms $m_2$, $m_3$, and $m_4$ are equal to 1, and meanwhile if $\mathbf{z}_4 = \mathbf{0}, \ldots, \mathbf{z}_{n+2} = \mathbf{0}$, the HOFTO in (17) will be equivalent to the ESO. The advantage of HOFTO over ESO is clarified in nonsmooth control; refer to, e.g., [26], [27]. In addition, if $\mathbf{z}_4 = \mathbf{0}, \ldots, \mathbf{z}_{n+2} = \mathbf{0}$, $m_2 = \frac{1}{2}$, $m_3 = \frac{1}{2}$, and $m_4 = 0$, the HOFTO in (17) will be equivalent to the STA observer.

## IV. Experimental Evaluations

In this section, a series of evaluations on a real robot manipulator (ER3A robot, made by Efort Intelligent Equipment Co., Ltd.) are reported to show the performance of our approach. The robotic system is depicted in Fig. 1, which consists of a motion control unit, a servo drive unit, and a basic machine unit. The motion control unit is implemented by a Beckhoff controller and developed in the MATLAB/Simulink environment through a model-based design (MBD) method. The servo drive unit is governed by a motion controller using the EtherCAT protocol. The basic machine unit is composed of six rotational joints and equipped with a 6-D force/torque sensor attached at the end-effector of the robot.

TABLE I
IDENTIFICATION RESULTS

| item | value | item | value | item | value | item | value |
|---|---|---|---|---|---|---|---|
| $\mu_1$ | 0.853 | $\mu_{17}$ | 0.284 | $\mu_{33}$ | 0.119 | $\mu_{49}$ | −0.000 |
| $\mu_2$ | 24.157 | $\mu_{18}$ | −0.197 | $\mu_{34}$ | 5.412 | $\mu_{50}$ | 0.010 |
| $\mu_3$ | 7.535 | $\mu_{19}$ | −0.273 | $\mu_{35}$ | 4.913 | $\mu_{51}$ | −0.001 |
| $\mu_4$ | 0.056 | $\mu_{20}$ | 0.732 | $\mu_{36}$ | −0.025 | $\mu_{52}$ | 0.002 |
| $\mu_5$ | 0.346 | $\mu_{21}$ | 1.910 | $\mu_{37}$ | 0.079 | $\mu_{53}$ | 0.003 |
| $\mu_6$ | 0.593 | $\mu_{22}$ | 1.274 | $\mu_{38}$ | 0.032 | $\mu_{54}$ | −0.001 |
| $\mu_7$ | 0.162 | $\mu_{23}$ | 13.127 | $\mu_{39}$ | 0.061 | $\mu_{55}$ | 0.021 |
| $\mu_8$ | −0.267 | $\mu_{24}$ | 9.924 | $\mu_{40}$ | 0.087 | $\mu_{56}$ | 0.573 |
| $\mu_9$ | −0.220 | $\mu_{25}$ | −0.445 | $\mu_{41}$ | 0.038 | $\mu_{57}$ | 1.946 |
| $\mu_{10}$ | 2.028 | $\mu_{26}$ | 0.119 | $\mu_{42}$ | −0.021 | $\mu_{58}$ | −0.006 |
| $\mu_{11}$ | 0.845 | $\mu_{27}$ | −0.038 | $\mu_{43}$ | 0.181 | $\mu_{59}$ | −5.136 |
| $\mu_{12}$ | 59.052 | $\mu_{28}$ | 0.110 | $\mu_{44}$ | 0.060 | $\mu_{60}$ | −13.643 |
| $\mu_{13}$ | 8.975 | $\mu_{29}$ | 0.061 | $\mu_{45}$ | 6.716 | $\mu_{61}$ | 0.053 |
| $\mu_{14}$ | 3.492 | $\mu_{30}$ | 0.044 | $\mu_{46}$ | 3.230 | $\mu_{62}$ | −0.492 |
| $\mu_{15}$ | −0.181 | $\mu_{31}$ | −0.023 | $\mu_{47}$ | 0.054 | $\mu_{63}$ | −1.143 |
| $\mu_{16}$ | 0.015 | $\mu_{32}$ | 0.096 | $\mu_{48}$ | −0.008 | $\mu_{64}$ | −0.013 |

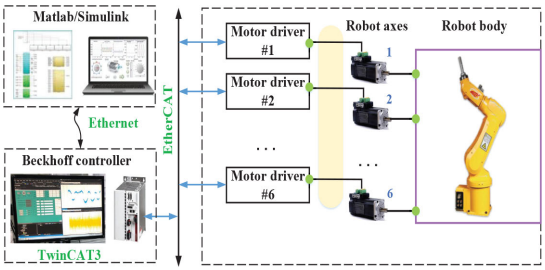


(a)

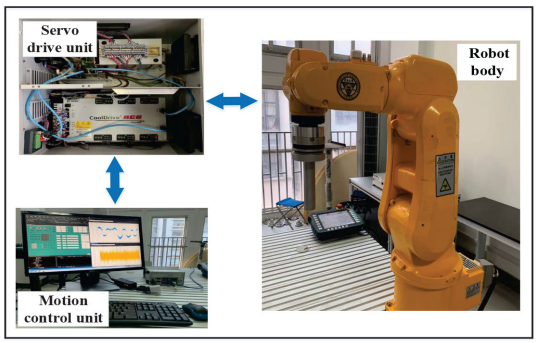


(b)

Fig. 1. Experiment setup. (a) Diagram of the robotics system. (b) Hardware architecture of the robot.

Following the dynamics identification approach in Section III-A, we can estimate the relevant dynamics model parameters, as listed in Table I, where all units are in SI units. The performance of the identified dynamics model on an excitation trajectory is shown in Fig. 2, where the blue curves denote the real torque inputs over the course of executing the excitation trajectory while the red curves correspond to the estimated torque with the identified dynamics model. We can see from the error curves (green curves) that the identification is satisfactory.

### A. Evaluations of Force Estimation

In order to evaluate the accuracy of force estimation, we consider a tracking task where the X-, Y-, and Z- components of the desired Cartesian trajectory are plotted in Fig. 3(b) and the corresponding 3-D trajectory is shown in Fig. 3(a). Here, the corresponding desired joint trajectory is determined by using the Jacobin-based inverse kinematics, as shown in Fig. 3(c). Note that the most challenging situation for interaction force estimation is when some joints are unchanged or at ultralow speeds. In Fig. 3(c), the fourth joint is almost unaltered, which leads to a challenging situation for interaction force estimation.

For the sake of comparison, we evaluate the traditional ESO-based estimation method whose gain parameters are set as $\mathbf{k}_1 = \mathrm{diag}\{8, 8, 5, 5, 5, 5\}$, $\mathbf{k}_2 = \mathrm{diag}\{50, 50, 40, 40, 40, 40\}$, and $\mathbf{k}_3 = \mathrm{diag}\{300,\ 300,\ 200,\ 200,\ 200,\ 200\}$. In addition, the disturbance-observer-based (DOB) method in [10] is also evaluated. Meanwhile, we choose the fourth-order HOFTO design, namely, $n = 2$, whose gain parameters for the proposed HOFTO-based estimation scheme are defined as $\mathbf{L}_1 = \mathrm{diag}\{22.3607, 22.3607, 21.6265, 20.8090, 20.8090, 20.8090\}$, $\mathbf{L}_2 = \mathrm{diag}\{22.101, 22.101, 21.1419, 20.083, 20.083, 20.083\}$, $\mathbf{L}_3 = \mathrm{diag}\{30, 30, 28.0624, 25.9808, 25.9808, 25.9808\}$, and $\mathbf{L}_4 = \mathrm{diag}\{440,\ 440,\ 385,\ 330,\ 330,\ 330\}$. Note that the parameter adjustment is mainly based on the recursive

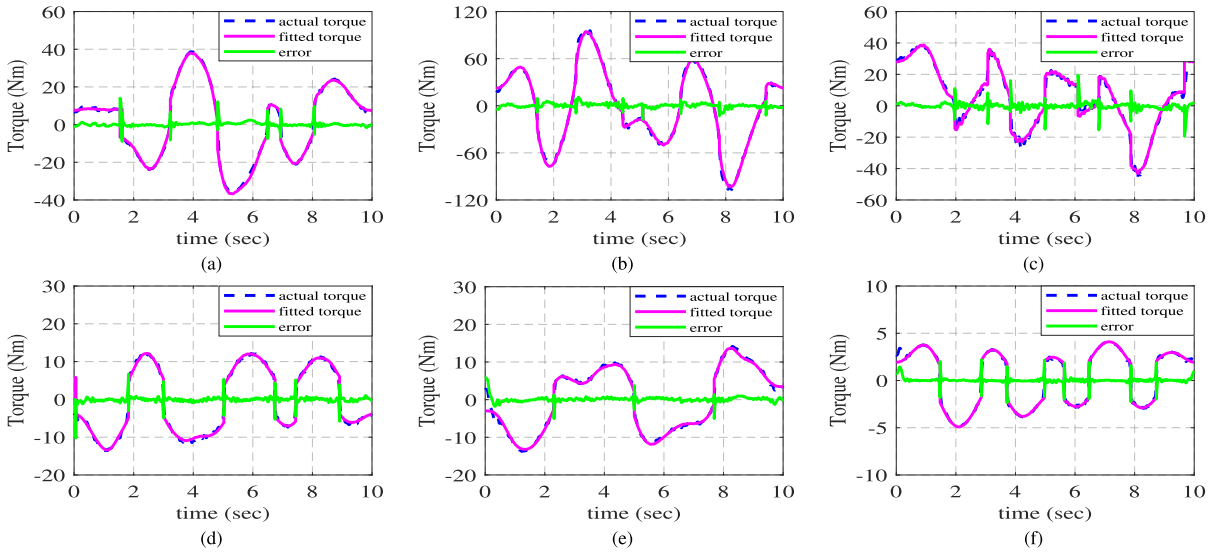


Fig. 2. Comparison between the measured and estimated torque. (a)–(f) First to sixth joints, where the blue dashed, red solid, and green solid curves depict the measured torque, estimated torque, and the corresponding torque errors, respectively.

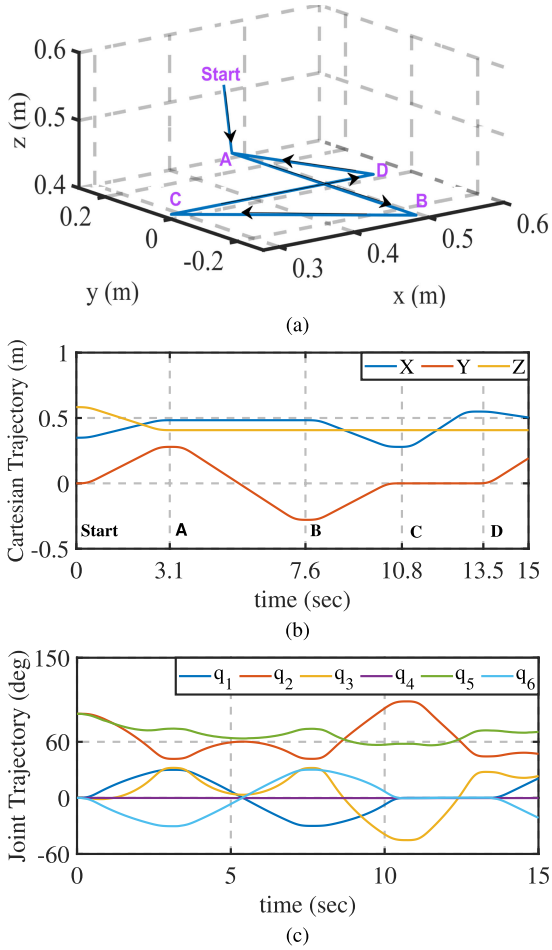


Fig. 3. (a) 3-D motion trajectory. (b)–(c) Trajectories in Cartesian space and joint space, respectively. $Start$, $A, B, C$, and $D$ separately mark the starting and desired points.

selection scheme introduced in [28] and supplemented by the trial-and-error method.

The estimated interaction forces by using the HOFTO, the ESO-based, and the DOB methods are shown in Fig. 4, where the real measured torque by using a torque/force sensor is provided as the baseline. It can be seen that the HOFTO method indeed has a more precise estimation compared to ESO-based and DOB approaches. Furthermore, to quantitatively assess our method, the performance indices including the offset value defined as the absolute of the mean value of estimating errors, the maximum absolute (MA) value representing the maximum of absolute value of a sequence of data, and the root-mean-squared (RMS) value denoting the square root of the average of squares of a set of data are taken into account. The quantitative evaluations are summarized in Table II, showing that HOFTO improves the estimation precision over ESO and DOB significantly. Note that, due to unmodeled dynamics and measurement noise, the proposed method still brings estimation errors, but these errors are trivial for human–robot interaction applications.

## B. Evaluations of Collision Detection

Collision detection is a very common task in industrial scenarios. In the event of a collision, it is often required to detect external contact forces. In our experiment, we block the end-effector of a robot when it collides with an obstacle.

During the collision, the response curves of the interaction force estimation in joint space and Cartesian space are shown in Figs. 5 and 6, respectively, from which we can observe that the proposed estimation strategy detects the external force effectively.

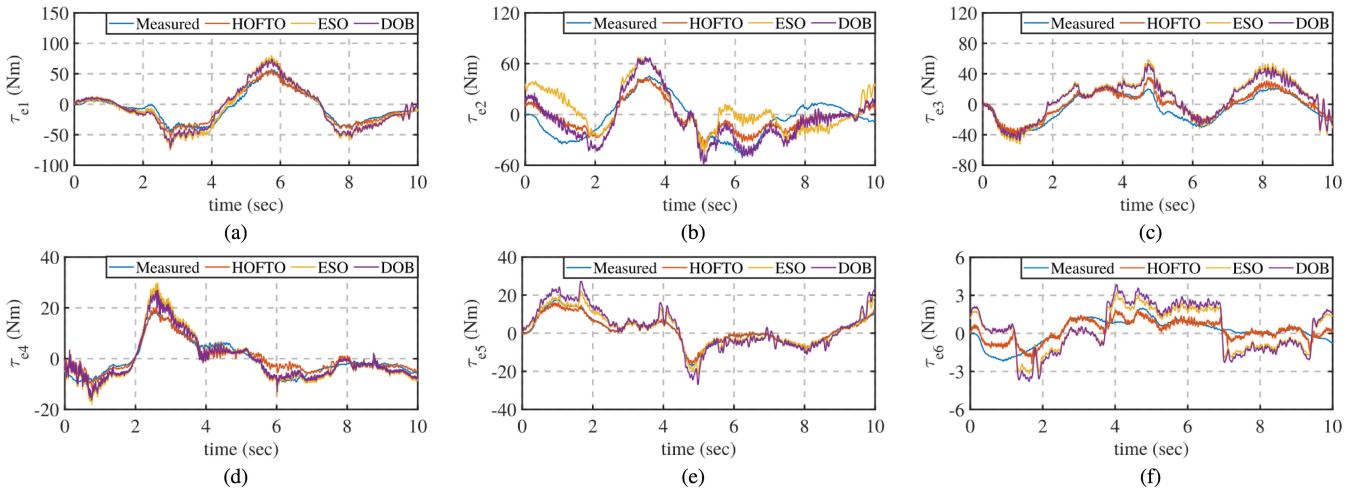


Fig. 4. Comparison among the HOFTO-based (red curve) method, the ESO-based (yellow curve) method, and the DOB (purple curve) method. (a)–(f) First to sixth joints, respectively. The blue curves depict the real measured external torque.

TABLE II
PERFORMANCE INDICES UNDER THREE ESTIMATION APPROACHES

| | $\tau_{e1}$ | | | $\tau_{e2}$ | | | $\tau_{e3}$ | | |
|---|---|---|---|---|---|---|---|---|---|
| | Offset | MA | RMS | Offset | MA | RMS | Offset | MA | RMS |
| *HOFTO* | 0.6566 | 19.0628 | 5.6758 | 1.4586 | 30.0325 | 13.7747 | 4.5513 | 29.8924 | 6.9009 |
| *ESO* | 2.0557 | 31.0833 | 10.7413 | 10.2418 | 60.2324 | 27.800 | 11.6811 | 39.0532 | 16.4946 |
| *DOB* | 1.8935 | 28.6627 | 10.6633 | 7.609 | 58.3107 | 20.1128 | 11.0636 | 34.5772 | 14.8554 |
| | $\tau_{e4}$ | | | $\tau_{e5}$ | | | $\tau_{e6}$ | | |
| | Offset | MA | RMS | Offset | MA | RMS | Offset | MA | RMS |
| *HOFTO* | 0.5386 | 9.4659 | 2.8030 | 0.0239 | 3.4266 | 0.9214 | 0.0885 | 2.1013 | 0.5057 |
| *ESO* | 1.1106 | 11.5670 | 4.3130 | 0.6496 | 9.1514 | 2.7173 | 0.1063 | 2.5020 | 1.3726 |
| *DOB* | 0.8419 | 10.1855 | 3.6928 | 1.1858 | 14.3877 | 4.3777 | 0.1560 | 2.9912 | 1.6311 |

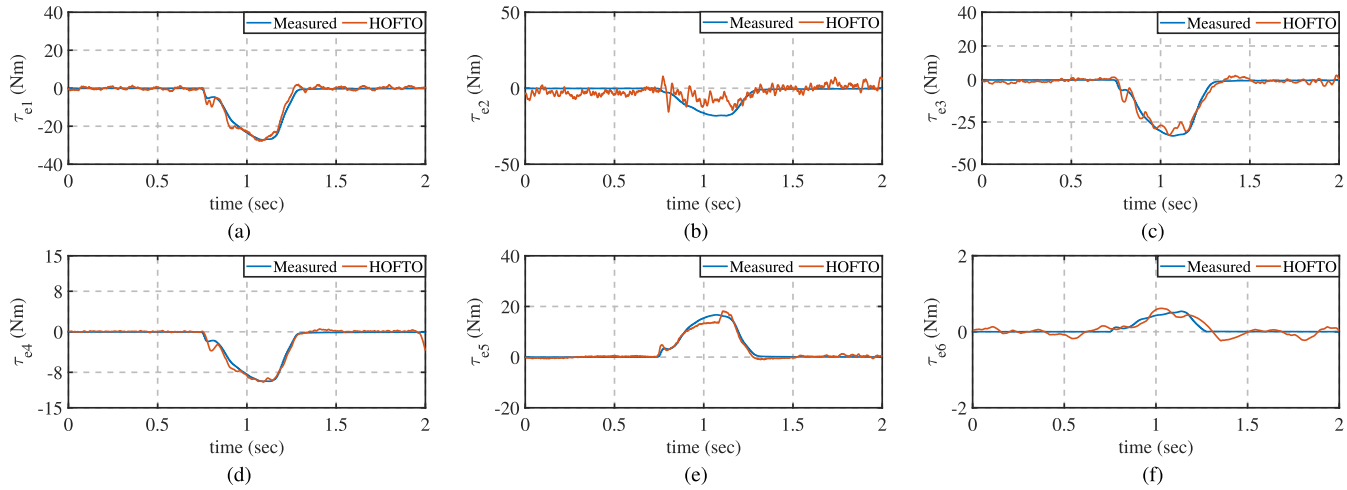


Fig. 5. Estimated and measured interaction force in collision detection. (a)−(f) First to sixth joints.

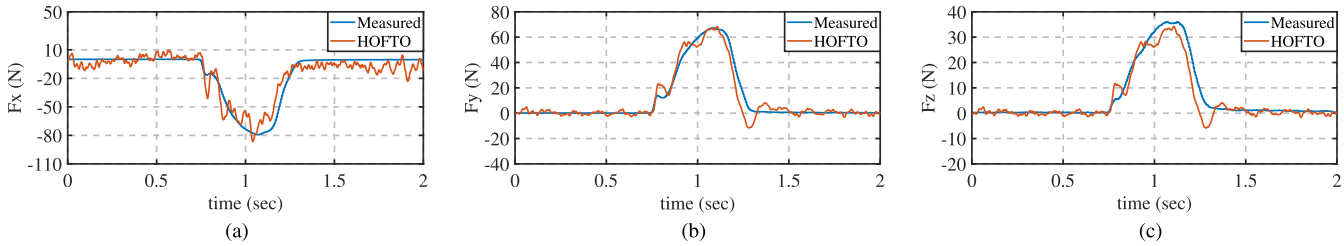


Fig. 6. Estimated and measured interaction force in collision detection. (a)–(c) $X$-, $Y$-, and $Z$- directions in Cartesian space.

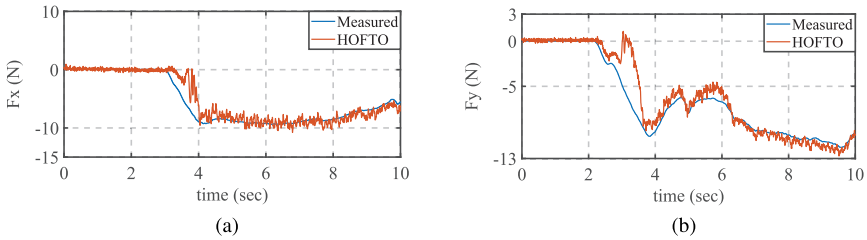


Fig. 7. (a) and (b) Traction tracking along the $X$- and $Y$- directions, respectively.

### C. Sensorless Drag Control

Impedance control is widely used in human–robot interaction scenarios [29], which can be expressed as

$$\mathbf{M}_a\ddot{\mathbf{X}}_d + \mathbf{B}_a\dot{\mathbf{X}}_d + \mathbf{K}_a\mathbf{X}_d = \mathbf{F}_e - \mathbf{F}_d \tag{33}$$

where $\mathbf{X}_d$ and $\mathbf{F}_d$ represent the desired position in Cartesian space and the contact force with the end-effector, respectively. $\mathbf{M}_a$, $\mathbf{B}_a$, and $\mathbf{K}_a$ denote the inertia matrix, damping matrix, and stiffness matrix of the target impedance model, respectively, and $\mathbf{F}_e$ is the interaction force.

With the estimated interaction forces, we realize the sensorless drag and teaching function by setting $\mathbf{K}_a = \mathrm{diag}\{\mathbf{0}_{1\times 6}\}$ and $\mathbf{F}_d = \mathbf{0}_{6\times 1}$ in (33), giving

$$\mathbf{M}_a\ddot{\mathbf{X}}_d + \mathbf{B}_a\dot{\mathbf{X}}_d = (\mathbf{J}^{\mathrm{T}})^{-1}\hat{\boldsymbol{\tau}}_e \tag{34}$$

with $\mathbf{J}$ being the jacobian matrix. In the procedure of traction, the estimated contact forces along the X- and Y- directions are shown in Fig. 7(a) and (b), respectively. Note that the chattering shown in Fig. 7 results from two main factors. First, the proposed HOFTO is essentially a nonsmooth and nonlinear observer, where the chattering is caused by the parameter adjustment, especially the fractional power term. When fractional power terms are 0, the proposed observer will become noncontinuous as the function $\mathrm{sig}(\cdot)$ in our observer degrades into the switching function $\mathrm{sign}(\cdot)$. In this case, chattering is the largest. When fractional power terms are 1, the proposed observer will become linearly continuous. In this case, the chattering can be avoided, but the finite time convergence cannot be guaranteed. Therefore, in our experiments the fractional power term is set as (0,1) as a trade-off between chattering and the finite time convergence. Second, measurement noise is a chattering-producing factor that cannot be ignored.

## V. Conclusion

Interaction force estimation was viewed as a vital research line in the context of force control. This article presented an observer for estimating the interaction forces applied to industrial robot manipulators. Following the procedure in this article, a finite-time convergent HOFTO was established. Through several evaluations on a real robotic manipulator, we demonstrated that the proposed nonlinear HOFTO is capable of estimating the interaction forces more precisely than ESO and performs well in various applications, including collision detection and impedance control.

## References

[1] B. Siciliano and L. Villani, *Robot Force Control*. Berlin, Germany: Springer Science & Business Media, 2012.

[2] S. Zhang, S. Wang, F. Jing, and M. Tan, "A sensorless hand guiding scheme based on model identification and control for industrial robot," *IEEE Trans. Ind. Informi.*, vol. 15, no. 9, pp. 5204–5213, Sep. 2019.

[3] P. Cao, Y. Gan, and X. Dai, "Model-based sensorless robot collision detection under model uncertainties with a fast dynamics identification," *Int. J. Adv. Robotic Syst.*, vol. 16, no. 3, pp. 1–15, 2019.

[4] E. Magrini, F. Flacco, and A. De Luca, "Estimation of contact forces using a virtual force sensor," in *Proc. Conf. Intell. Robots Syst.*, 2014, pp. 2126–2133.

[5] A. Wahrburg, J. Bös, K. D. Listmann, F. Dai, B. Matthias, and H. Ding, "Motor-current-based estimation of cartesian contact forces and torques for robotic manipulators and its application to force control," *IEEE Trans. Automat. Sci. Eng.*, vol. 15, no. 2, pp. 879–886, Apr. 2018.

[6] C. Yang, G. Peng, L. Cheng, J. Na, and Z. Li, "Force sensorless admittance control for teleoperation of uncertain robot manipulator using neural networks," *IEEE Trans. Syst., Man, Cybern. Syst.*, vol. 51, no. 5, pp. 3282–3292, May 2021

[7] S. Haddadin, A. De Luca, and A. Albu-Schäffer, "Robot collisions: A survey on detection, isolation, and identification," *IEEE Trans. Robot.*, vol. 33, no. 6, pp. 1292–1312, Dec. 2017.

[8] J. Na, B. Jing, Y. Huang, G. Gao, and C. Zhang, "Unknown system dynamics estimator for motion control of nonlinear robotic systems," *IEEE Trans. Ind. Electron.*, vol. 67, no. 5, pp. 3850–3859, May 2020.

[9] K. S. Eom, I. H. Suh, W. K. Chung, and S.-R. Oh, "Disturbance observer based force control of robot manipulator without force sensor," in *Proc. Conf. Robot. Automat.*, vol. 4, 1998, pp. 3012–3017.

[10] E. Sariyildiz and K. Ohnishi, "On the explicit robust force control via disturbance observer," *IEEE Trans. Ind. Electron.*, vol. 62, no. 3, pp. 1581–1589, Mar. 2015.

[11] E. Sariyildiz and K. Ohnishi, "Stability and robustness of disturbance-observer-based motion control systems," *IEEE Trans. Ind. Electron.*, vol. 62, no. 1, pp. 414–422, Jan. 2015.

[12] G. Sebastian, Z. Li, V. Crocher, D. Kremers, Y. Tan, and D. Oetomo, "Interaction force estimation using extended state observers: An application to impedance-based assistive and rehabilitation robotics," *IEEE Robot. Automat. Lett.*, vol. 4, no. 2, pp. 1156–1161, Apr. 2019.

[13] G. Garofalo, N. Mansfeld, J. Jankowski, and C. Ott, "Sliding mode momentum observers for estimation of external torques and joint acceleration," in *Proc. Conf. Robot. Automat.*, 2019, pp. 6117–6123.

[14] M. W. Spong, "On the robust control of robot manipulators," *IEEE Trans. Autom. Control*, vol. 37, no. 11, pp. 1782–1786, Nov. 1992.

[15] S. Li, J. Yang, W.-H. Chen, and X. Chen, *Disturbance Observer-Based Control: Methods and Applications*. Boca Raton, FL, USA: CRC Press, 2014.

[16] C. Qian and W. Lin, "A continuous feedback approach to global strong stabilization of nonlinear systems," *IEEE Trans. Autom. Control*, vol. 46, no. 7, pp. 1061–1079, Jul. 2001.

[17] Y. Han, J. Wu, C. Liu, and Z. Xiong, "An iterative approach for accurate dynamic model identification of industrial robots," *IEEE Trans. Robot.*, vol. 36, no. 5, pp. 1577–1594, Oct. 2020.

[18] L. Simoni, M. Beschi, G. Legnani, and A. Visioli, "Friction modeling with temperature effects for industrial robot manipulators," in *Proc. Conf. Intell. Robots Syst.*, 2015, pp. 3524–3529.

[19] A. Wahrburg *et al.*, "Modeling speed-, load-, and position-dependent friction effects in strain wave gears," in *Proc. Conf. Robot. Automat.*, 2018, pp. 2095–2102.

[20] S. Wolf and M. Iskandar, "Extending a dynamic friction model with nonlinear viscous and thermal dependency for a motor and harmonic drive gear," in *Proc. Conf. Robot. Automat.*, 2018, pp. 783–790.

[21] M. Gautier and W. Khalil, "Direct calculation of minimum set of inertial parameters of serial robots," *IEEE Trans. Robot. Automat.*, vol. 6, no. 3, pp. 368–373, Jun. 1990.

[22] H. Mayeda, K. Yoshida, and K. Osuka, "Base parameters of manipulator dynamic models," in *Proc. Conf. Robot. Automat.*, 1988, pp. 1367–1372.

[23] J. Wu, J. Wang, and Z. You, "An overview of dynamic parameter identification of robots," *Robot. Comput.-Integr. Manuf.*, vol. 26, no. 5, pp. 414–419, 2010.

[24] J. Jin and N. Gans, "Parameter identification for industrial robots with a fast and robust trajectory design approach," *Robot. Comput.-Integr. Manuf.*, vol. 31, pp. 21–29, 2015.

[25] H. Du, C. Qian, S. Yang, and S. Li, "Recursive design of finite-time convergent observers for a class of time-varying nonlinear systems," *Automatica*, vol. 49, no. 2, pp. 601–609, 2013.

[26] C. Zhang, Y. Yan, C. Wen, J. Yang, and H. Yu, "A nonsmooth composite control design framework for nonlinear systems with mismatched disturbances: Algorithms and experimental tests," *IEEE Trans. Ind. Electron.*, vol. 65, no. 11, pp. 8828–8839, Nov. 2018.

[27] P. Lin, C. Zhang, J. Wang, C. Jin, and P. Wang, "On autonomous large-signal stabilization for islanded multibus dc microgrids: A uniform nonsmooth control scheme," *IEEE Trans. Ind. Electron.*, vol. 67, no. 6, pp. 4600–4612, Jun. 2020.

[28] A. Levant, "Higher-order sliding modes, differentiation and output-feedback control," *Int. J. Control*, vol. 76, no. 9–10, pp. 924–941, 2003.

[29] J. Duan, Y. Gan, M. Chen, and X. Dai, "Adaptive variable impedance control for dynamic contact force tracking in uncertain environment," *Robot. Auton. Syst.*, vol. 102, pp. 54–65, 2018.


**Linyan Han** received the M.Sc. degree in control theory and control engineering from the Nanjing University of Aeronautics and Astronautics, Nanjing, China, in 2017. She is currently working toward the Ph.D degree with the School of Automation, Southeast University, Nanjing, China.

Her research interests include force control, position control, nonlinear control theory, and their applications to robotic systems.

**Jianliang Mao** received the B.Sc., M.Sc., and Ph.D. degrees from the School of Automation, Southeast University, Nanjing, China, in 2011, 2014, and 2018, respectively.

From 2018 to 2021, he was with the Research and Development Institute, Estun Automation Co., Ltd., Nanjing, China. He is currently with the College of Automation Engineering, Shanghai University of Electric Power, Shanghai, China. His research interests include interactive control and visual servoing control of robotic manipulators.

**Pengfei Cao** received the B.S. degree in automatic control in 2014 from Southeast University, Nanjing, China, where he is currently working toward the Ph.D. degree.

His research interests include force control, human–robot interaction, and motion planning.

**Yahui Gan** received the B.Eng. degree in automation from Shandong University, Jinan, China, in 2007, and the Ph.D. degree in control theory and control engineering from Southeast University, Nanjing, China, in 2014.

Since 2014, he has been with the School of Automation, Southeast University, where he is currently an Associate Professor. His research interests include robot intelligent control system, human–robot interaction, and multiple robots cooperation.

**Shihua Li** (Fellow, IEEE) received the B.S., M.S., and Ph.D. degrees in automatic control from Southeast University, Nanjing, China, in 1995, 1998, and 2001, respectively.

Since 2001, he has been with the School of Automation, Southeast University, where he is currently a Professor and the Director of Mechatronic Systems Control Laboratory. His research interests include modeling, analysis, and nonlinear control theory with applications to mechatronic systems, including manipulator, robot, ac motor, power electronic systems, and others.